

Label up: Learning Pulmonary Embolism Segmentation from Image Level Annotation through Model Explainability

Florin Condrea, Saikiran Rapaka, Marius Leordeanu

Abstract—Pulmonary Embolisms (PE) are a leading cause of cardiovascular death. Computed tomographic pulmonary angiography (CTPA) stands as the gold standard for diagnosing pulmonary embolisms (PE) and there has been a lot of interest in developing AI-based models for assisting in PE diagnosis. Performance of these algorithms has been hindered by the scarcity of annotated data, especially those with fine-grained delineation of the thromboembolic burden. In this paper we attempt to address this issue by introducing a weakly supervised learning pipeline, that leverages model explainability to generate fine-grained (pixel level) masks for embolisms starting from more coarse-grained (binary, image level) PE annotations. Furthermore, we show that training models using the automatically generated pixel annotations yields good PE localization performance. We demonstrate the effectiveness of our pipeline on the large-scale, multi-center RSPECT augmented dataset for PE detection and localization.

Index Terms—Pulmonary embolism detection, CT pulmonary angiography, deep neural networks, weakly supervised learning, model explainability

I. INTRODUCTION

Pulmonary embolisms (PEs), characterized by blood clots (thrombi) in the pulmonary arteries, constitute a significant public health challenge as the third most prevalent cardiovascular syndrome globally, following myocardial infarction and stroke [1]. The incidence rate ranges from 39-115 per 100,000 individuals for PEs and 53-166 per 100,000 for the related deep vein thrombosis [2], [3], resulting in approximately 300,000 annual fatalities in the United States alone [3]. This health burden is expected to increase due to the association with Covid-19 infections [4] and the documented upward trend in PE occurrence [2], [5]–[7]. The critical nature of PE diagnosis is underscored by the fact that 34% of deaths occur either suddenly or within hours of the acute event, before

treatment can be administered [8]. Given this urgency and the increasing hospital workload [9], [10], there is a pressing need for rapid and accurate patient triage and prioritization systems. CT pulmonary angiography (CTPA) remains the diagnostic gold standard for PE detection [11], positioning this medical challenge within the scope of modern computer vision applications, particularly those utilizing deep neural networks. Deep neural networks, especially convolutional neural networks (CNNs), have established themselves as powerful tools for pattern recognition and detection in visual tasks [12]–[15]. Their effectiveness extends across various medical imaging applications, yielding impressive results in diagnosing conditions such as Chronic Obstructive Pulmonary Disease (COPD) [16], Covid-19 [17], and intracranial hemorrhage [18] using CT scans. These networks have also demonstrated success across other imaging modalities, including radiography [19], [20] and magnetic resonance imaging (MRI) [21], [22].

While the topic of segmentation in the medical domain has been well covered [23]–[25] and many recent publications cover the topic of pulmonary embolism classification either on slice level or study level [26]–[31], development of detailed localization or segmentation of the PEs [28], [32], [33] is lagging behind. This could be attributed to the scarcity of fine-grained annotations for this task due to the expensive annotation process. The recently released public RSPECT augmented large scale dataset [34] for PE localization will allow more contribution in this space.

Main Contribution: We introduce a weakly supervised generalist pipeline that is able to generate fine-grained annotations, in our case PE segmentations, starting from a coarser grained annotations, in our case image level PE binary labels. The pipeline relies on model explainability to generate iteratively refined annotations. Our contributions in this paper are threefold:

- 1) We provide a weakly supervised generalist pipeline for improving the granularity of annotations, in our case from image level to pixel level. We evaluate the quality of the generated annotations on the RSPECT augmented dataset [34], demonstrating that the pipeline is capable of localization even on challenging tasks such as pulmonary embolism detection.
- 2) A baseline deep learning solution for PE localization on the novel RSPECT augmented dataset [34].
- 3) A model trained successfully on the weakly super-

Manuscript sent for review on 18 February 2023. Marius Leordeanu was supported in part by the EU Horizon project ELIAS (Project ID: 101120237).

Author F. Condrea is with the Institute of Mathematics of the Romanian Academy "Simion Stoilow" and Advanta, Siemens SRL, 15 Noiembrie Bvd, 500097 Brasov. (email: florin.condrea@siemens.com)

Author S. Rapaka is with the Siemens Healthineers, 08540 Princeton, NJ, USA. (email: saikiran.rapaka@siemens-healthineers.com)

Author M. Leordeanu is with the Institute of Mathematics of the Romanian Academy "Simion Stoilow", Advanta, Siemens SRL, 15 Noiembrie Bvd, 500097 Brasov, Romania and Polytechnic University of Bucharest. (email: leordeanu@gmail.com)

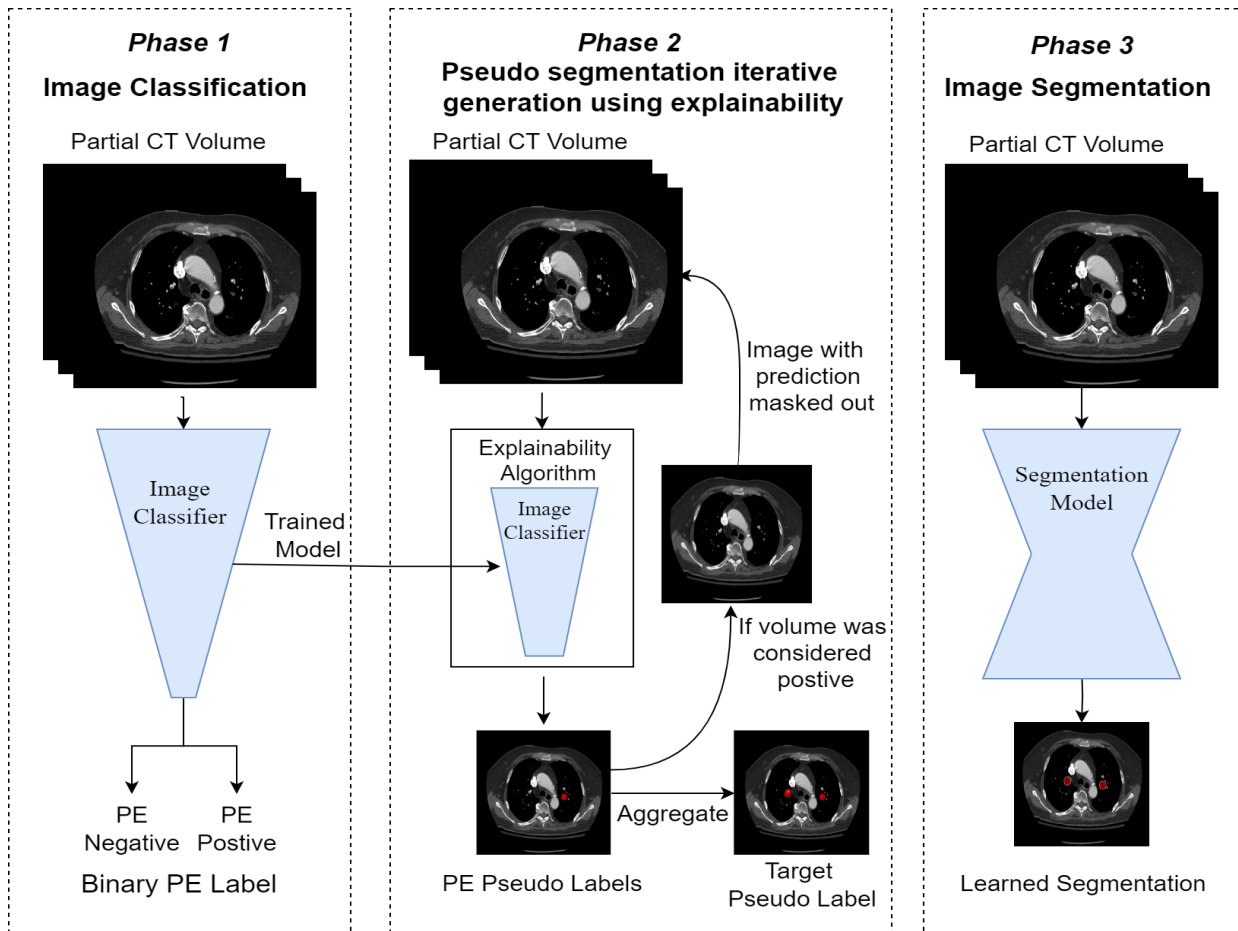


Fig. 1. Our proposed pseudo-label multistage pipeline. In Stage 1, a slice level classifier is trained to predict if a stack of slices is positive. In Stage 2, the trained classifier, together with integrated gradients algorithm, predict the location of PEs. After each iteration, the predicted zones are masked out, and volume fed back into the network. Process repeats until PEs are no longer detected and all predictions are aggregated into pseudo-labels. In Stage 3, a deep learning segmentation network is trained on the pseudo-labels.

vised generated annotations on the RSPECT augmented dataset [34], demonstrating that the pipeline is capable of generating annotations to be further used in the training of finegrained models.

II. RELATED WORK

Previous research has explored the development of Computer Assisted Detection (CAD) systems for Pulmonary Embolisms (PE) through two main methodological approaches. Early studies focused on traditional image processing techniques, utilizing segmentation and thresholding methods [35]–[38]. More recent investigations have leveraged Deep Learning approaches, particularly convolutional neural networks (CNNs) [26]–[29]. More recent has focused on PE localization [28], [32], [39], [40], allowing for a more finegrained evaluation of model performance.

Model Explainability has become a point of interest in machine learning in recent years, many approaches [41]–[43] being developed to best capture the sources of information in an input. While widely adopted for qualitative examples, recent work [44]–[47] have adopted feature use heatmaps generated by explainability methods and refined them into weakly supervised segmentations.

There are two papers of special interest for our work [33], [44]. In the former, Gonzalez et al [44] set the groundwork for our iterative weakly supervised learning pipeline, which we further develop. They obtain weakly supervised segmentation for retinal diseases in 2D color fundus images by iteratively refining the prediction of various explainability methods. They rely on an additional model to inpaint the areas previously predicted, forcing the network to rely on other image cues.

In the latter, Pu et al. [33] represent our main point of comparison, their method also training a deep learning method on pseudo-labels for PE localization. In their work, they rely heavily on anatomical information and an external model for pulmonary artery segmentation. In the artery segmentation, they search using classical computer vision algorithms for areas matching the contrast profile of a PE, thus obtaining segmentation of likely PEs.

III. OUR METHOD

Our weakly supervised learning pipeline, taking the form of an offline teacher - online student, capable of training a segmentation model starting from image level annotation is composed of three stages, to be presented in detail in the following section:

- 1) Classification model for image level classification, trained on initial human annotations
- 2) Explainability module for weakly supervised segmentation generation, acting as an offline teacher, to obtain fine-grained weakly supervised annotations
- 3) Segmentation model for pixel level classification, acting as an online student, trained on fine-grained WSL annotations

A. Slice level Classifier.

As suggested in recent publications [31], [48], [49], a 2.5D CNN has been employed as an image level classifier. We closely follow the baseline training recipe from a recent solution [31] trained and tested on the RSPECT PE classification data set [50], where a 2.5D EfficientNetV2-L is trained. The input of the network is a 3D minivolume containing consecutive slices, resulting in a shape of (512,512,7), and the target label corresponding is the label of the center slice. Of special interest from the baseline [31] for improving explainability performance of our pipeline is the augmentation scheme and final pooling layer used. The augmentation scheme contains an aggressive form of cutout augmentations taking out random parts of the input, which they show improves performance significantly, while also allowing input masking during our second stage. The pooling layers is MaxPool, which as noted by previous work [51], improves the granularity of explainability methods, allowing for more focused explainability heatmaps.

Training Details. The network input is of size (512,512,7), to which a HU windowing of center 100, and width 400 is applied. Train data is augmented as in HopNet paper [31], with "monai.transforms.RandCoarseDropout(max_holes = 2, holes = 1, max_spatial_size = (200,200,-1), spatial_size = (40,40,-1), prob = 0.4, fill_value=0)" standing out, making the model robust to missing information. For additional robustness, model was trained using Mix Up augmentation [52]. The network itself is EfficientNetV2-L, pretrained on Imagenet21k [53], imported from Timm library [54]. It has been trained using AdamW optimizer [55], over 50000 iterations, using Focal Loss with a base learning rate of 1e-3, warm up of 1000 iterations and linear decay to 1e-7.

B. Explainability generated pseudo-labels.

To generate our weakly supervised annotations, we rely on the Integrated Gradients [41] model explainability algorithm, implemented in the Captum library [56]. Previous work in this space [44] has evaluated several popular algorithms such as saliency [57], guided backpropagation [58], integrated gradients (IG) [41], Grad-CAM [42], and guided Grad-CAM [42], and their results suggest IG to be a good method, especially for small objects such as pulmonary embolisms.

Our method, given a 3D mini-volume, predicts using Integrated Gradients and our slice level model a 3D heatmap and a PE probability for the central slice of the volume. The heatmap represents the regions of the image that were most influential in the PE positive prediction of the model. In the case of PEs, the only reliable cue for PE positivity is the PE

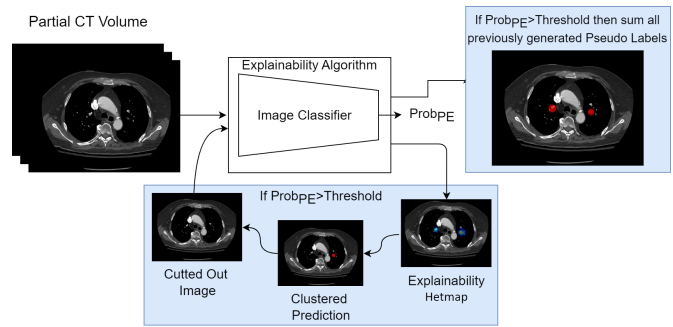


Fig. 2. Explainability module of our pipeline. Each mini volume of 7 slices of a study is classified, and if positive, Integrated Gradients is applied to obtain a feature use representing a PE probability heatmap. The heatmap is binarized in distinct clusters using Hysteresis thresholding, and masked out in the input volume, the classification process repeats until volume is classified negative. To generate for the whole study, sliding window with weighted aggregation is applied over all the predicted clusters.

itself [59], thus the PE, if present, will most likely attract all the weight of the heatmap, thus making the explainability heatmap a localization heatmap.

To transform the heatmap into a segmentation, a thresholding akin to Hysteresis thresholding. It uses two thresholds to improve segmentation. It involves an upper threshold, where pixels with intensity values above it are classified as part of the object, and a lower threshold, where pixels are included only if they are connected to those above the upper threshold. In our case, taking advantage of PE properties, where PEs are usually oval and the center is easier to recognize, we consider a neighborhood of (15,15,5) pixels around pixels over the high threshold, and anything within that area over the low threshold as part of the cluster. Although this approach may miss parts of thin long-tailed PEs, it is robust to clustered PEs whose heat maps may intersect.

Finally, to obtain a heatmap for the entire CTPA volume, the algorithms is applied using a sliding window centered on each slice. For their aggregation, each slice is the weighted sum parametrized by a Gaussian ($\sigma = 0.8$) of the neighbor slices.

To improve the predictions, especially in the case of multiple PEs in a mini-volume as in Fig. 3, an iterative refinement process has been adopted. Multiple cluster predictions are performed, after each iteration, predicted clusters are masked using zeros out of the CTPA volume. This process is repeated until either no more PEs are detected, new segmentations have a volume under 50 voxels or 10 repetitions have been reached. First condition would mean no more steps are required, and the other two conditions are required as computational restrictions. The final segmentation is obtained through the union of all the prediction over the iterations. Similar iterative procedures have been employed by Gonzalez et al [44], a key difference is that they require a separate in-painting model to mask out their previous detections, while we, through the CutOut training of our slice classifier, are able to simply zero out previous predictions.

To further improve the performance of the explainability module, two types of voting at heatmap level have been adopted by generating multiple predictions for each volume. A

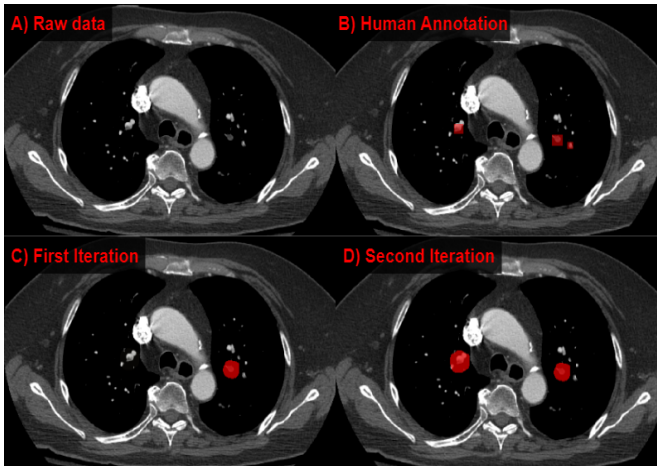


Fig. 3. Qualitative example of iterative improvement displaying the discovery of new PEs through the iterative process. A) Raw study B) Human Ground Truth C) First Iteration D) Second Iteration

first form of augmentation leverages references, a secondary input taken by integrated gradients [41]. A second form of augmentation is SmoothGrad [43], where the input image has Gaussian noise added, and the final prediction is averaged over multiple noise instances. As demonstrated by previous work [60], averaging over multiple random noise samples, either at image level or reference level, improves the robustness of integrated gradients. Our refinement loop is described in Algorithm 1.

Pseudo-label filtering. To take advantage of the adjustable operating point of our pseudo-label pipeline, a high sensitivity operating point is used in combination with result post processing to reduce False Positives. For each cluster, a size and location filter is applied. All clusters under a size threshold are removed, and all clusters that have a distance larger than a distance threshold from the center of the study are removed. For the distance metric, we use Euclidian 2D distance, but both 3D and 2D distance report similar performance. While both values are determined empirically, size filter corresponds to filtering very small predictions produced by sporadic predictions, and distance threshold limits PE search space to the lung area.

Algorithm 1: Our Iterative Segmentation Algorithm

Input: vol, clf, expl_mod, clf_thresh, heatmap_thresh, iter_limit
Output: agg_seg

```

1 segs  $\leftarrow$  [] curr_vol  $\leftarrow$  vol iter  $\leftarrow$  0 masked  $\leftarrow$   $\infty$ ;
2 while (clf.predict(curr_vol) > clf_thresh) and (iter < iter_limit) and (masked > heatmap_thresh) do
3   iter  $\leftarrow$  iter + 1;
4   heatmap  $\leftarrow$  expl_mod.explain(clf, curr_vol);
5   seg  $\leftarrow$  clustering(heatmap);
6   masked  $\leftarrow$  sum(seg);
7   curr_vol  $\leftarrow$  curr_vol * (1 - seg);
8   segs.append(seg);
9 end
10 agg_seg  $\leftarrow$  union(segs);

```

C. Deep learning segmentation model.

For our third stage, the deep learning segmentation model uses a standard DynUNET from Monai framework [61], a variant of the popular nnUnet architecture [23]. Of special interest for our training using pseudo-label are methods that encourage robustness to noisy labels. For this purpose, we employ Generalized Dice Loss [62] and Mixup data augmentation [52], both having shown to increase model stability and performance when training on noisy labels.

Model takes as input a (128,128,64) voxel patch, and outputs a PE probability heatmap. To obtain a heat map for the entire study, a sliding window algorithm is applied with step (64,64,32) and prediction aggregation via a weighted average parametrized by a scaled Gaussian ($\sigma = 0.25$).

Training Details. The network input is of size (128,128,64), to which a HU windowing of center 100, and width 400 is applied. The same augmentation scheme as for Stage 1 is applied, with the addition of a RandomCrop of size (128,128,64) and the exclusion of Random Cutout. Model itself is a standard DynUnet from Monai framework [61]. Model is trained with balanced sampling, using Generalized Dice Loss [62]. The training schedule is of 50,000 iterations with a batch size of 32 using AdadW optimizer [55], with a starting learning rate of $1e-4$, a warm up of 1000 iterations, and linear decay to $1e-7$.

IV. RESULTS

We train all our 3 stages on the RSPECT dataset [50], adding an additional private dataset to stage 3, and evaluate the performance on the RSPECT augmented dataset [34].

Datasets. RSPECT dataset [50] has been released by the Radiological Society of North America as part of a Kaggle challenge [63], contains 12,195 studies (CT scan volumes) with a positivity rate of 30.4%, with slice-level annotations regarding the presence of a pulmonary embolism, and several other study-level annotations. A subset of 7279 studies have been published with annotations as part of a Kaggle challenge, further referred to as RSPECT challenge training dataset.

The RSPECT [34] augmented released subsequently contains a subset of 445 PE positive studies from the initial RSPECT challenge training dataset [50]. For each study, PEs are annotated in each slice using a 2D bounding box, and a total of 30243 bounding boxes have been annotated. For our segmentation pipeline, we converted said bounding boxes to segmentation masks. Unfortunately, due to the nature of bounding boxes, some resulting annotations are over-segmented, as shown in Fig. 4.

We augmented our training set with an additional private dataset containing 6,005 studies, of which 27% were positive cases.

For our experiments, we trained our models on RSPECT challenge training and our private data. To avoid data bleeding, studies also present in RSPECT augmented have been excluded from training, resulting in a training set of 6824 studies, with a positivity of 25.8%. We used the RSPECT augmented dataset for testing both classification and localization, as it contains higher quality, finer-grained annotations

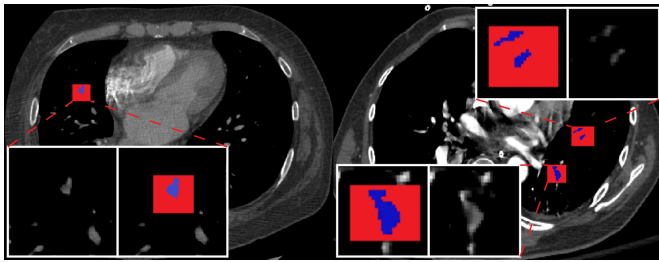


Fig. 4. Qualitative example of mismatch between bounding box annotations in red, and actual PE segmentations in blue. While the red annotations are well designed for object detection tasks evaluation, they are not adequate for segmentation evaluation. As such, we opt for evaluating our performance through F1 score for bounding box matching instead of segmentation Dice.

Metric For our first pipeline stage of PE slice classification, we rely on the AUC-ROC and F1 score metrics, both representing popular metrics for this task that reflect well the overall performance of the model.

For the 2nd and 3rd stages involving localization via segmentation, we use metrics that reflect the detection of PEs on finding/PE level using sensitivity, PPV and F1. These metrics align with those used in state-of-the-art solutions [28], [33], [39], [40]. We adopt the same cluster matching as Pu et al. [33], given that their training protocol on pseudo-labels is the closest to our own, and represent our main point of comparison, besides our extensive ablation studies. In their experiments, they consider that a detection and PE are matched whenever they intersect. Matched annotations are considered TPs, while unmatched annotations and detections are considered FNs, FPs respectively. Same metric is also used by Zhu et al [39].

Since RSPECT augmented [34] uses bounding box annotations that do not precisely outline PEs, traditional segmentation metrics like segmentation Dice or IOU are not suitable. Although Dice and F1 score have the same mathematical formula, we use F1 for our localization metrics to avoid confusion with segmentation metrics. Examples of mismatch between bounding boxes and actual segmentations are displayed in Fig. 4.

TABLE I

SLICE PREDICTOR PERFORMANCE. OUR FIRST STAGE MODEL ACHIEVES AUCROC PERFORMANCE IN THE STATE-OF-THE-ART RANGE, INDICATING IT IS ADEQUATELY TRAINED FOR THE FOLLOWING STAGE.

Model	Dataset size	F1	AUCROC
Xu et al. [48]	6,279	-	96.4
Ajmera et al. [64]	942	37.0	94.0
Ma et al. [30]	5,292	-	93.0
Ours	6,824	75.1	97.1

A. Image level classifier.

For the initial stage, we trained our 2.5D classifier on 6,824 studies, in order to obtain a future performing model for the next stage. Due to testing only on the fully positive subset of RSPECT [50], marked as a validation set, we report only slice-level performance. We obtain a slice-level performance AUCROC 97.08% and an F1 score of 75.11%, which, while

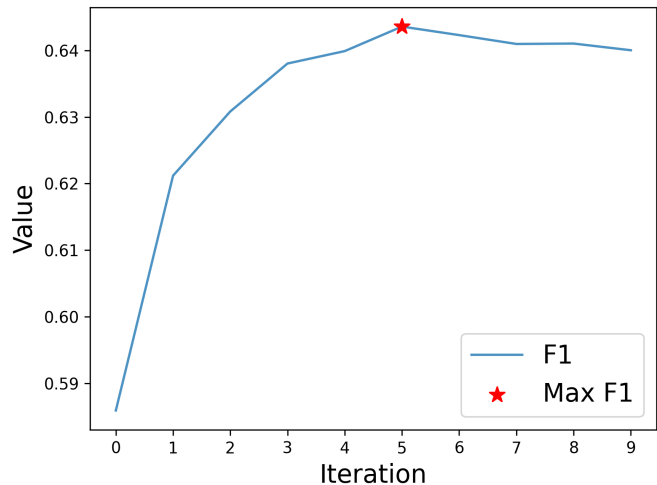


Fig. 5. Iterative improvement of F1 performance. Each iteration improves sensitivity and decreases PPV through the discovery of new PEs, balancing out after 6 iterations, obtaining maximum F1 score. Afterwards sensitivity and recall diverge, starting to slightly lower F1.

in different test datasets, is similar to other state-of-the-art methods [48]. Further comparisons are provided in Table I.

B. Weakly supervised segmentation.

For our weakly supervised segmentation model, we report PE localization performance with respect to bounding box matching. We perform several ablation studies, to showcase the improvements obtained by each of our contributions.

Iterative refinement. In Table II we report numbers for our iterative process, showing that significant improvements of 5.8 % F1 score can be obtained using iterative refinement. This is consistent for both scenarios of using 1 reference or 5 reference Integrated Gradients. The improvements are obtained through the discovery of new PEs by covering the previous ones. This is confirmed by the large increase in

TABLE II

STAGE 2 ITERATIVE REFINEMENT. SIGNIFICANT IMPROVEMENTS IN PERFORMANCE ARE OBTAINED THROUGH ITERATIVE REFINEMENT. THROUGH REPEATED MASKING AND PREDICTION, NEW PEs ARE DETECTED, AS DEMONSTRATED BY THE INCREASING SENSITIVITY. A TRADE-OFF IS CREATED BY THE DECREASING PPV, AND AN OPTIMUM F1 SCORE IS OBTAINED AFTER A COUPLE OF ITERATIONS.

References	Iteration	Sensitivity	PPV	F1
1	1	50.8	68.8	58.4
1	10, best	63.5	64.2	63.8
5	1	48.3	74.5	58.6
5	6, best	58.4	71.6	64.4

TABLE III

STAGE 2 CLUSTER FILTERING. TO IMPROVE PERFORMANCE, THE INITIAL OPERATING POINT OF THE PIPELINE IS SET TO FAVOR A HIGH SENSITIVITY, WHICH IS SUBSEQUENTLY BALANCED THROUGH CLUSTER FILTERING. FILTERING SIGNIFICANTLY IMPROVES F1 SCORE FOR BOTH SINGLE AND MULTI REFERENCE INTEGRATED GRADIENTS INFERENCE.

References	Filtered	Sensitivity	PPV	F1
1	×	65.1	45.1	53.3
1	✓	63.5	64.2	63.9
5	×	59.3	49.0	53.6
5	✓	58.4	71.6	64.4

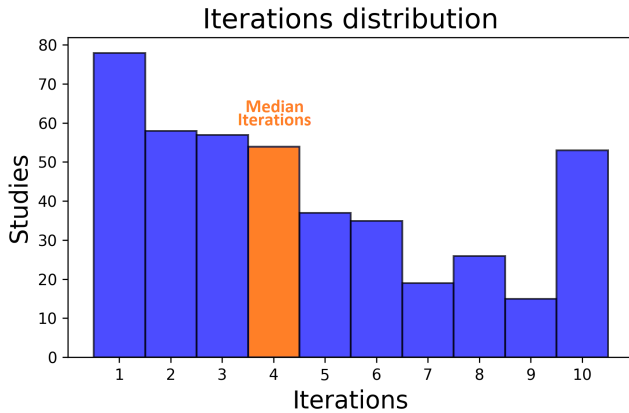


Fig. 6. Distribution of required WSL iterations. Most studies require only a couple of refinement iterations, with 15% requiring none. Required iterations steadily decreases due to no longer detecting PEs. The hard limit of 10 iterations creates a peak at the tail of the graph, indicating many studies would keep refining, although the overall performance decreases as shown in Fig. 5.

sensitivity, of 6.7% and 10.1% for 1 reference, 5 references respectively. While the prediction of additional clusters allows for additional False Positive, leading to lowering the PPV by 4.6% and 2.9%, this is far outweighed by the increased sensitivity.

The evolution of the F1 score can be observed in Fig. 5, with F1 peaking after 6 refinement iterations when sensitivity and PPV are balanced, after which it starts declining due to sensitivity and PPV diverging. The biggest boost in performance is caused by the first couple of iterations, and the iterative process terminates for most cases after a couple of steps, as shown in Fig 6.

Since not all studies require the same number of refinement steps, our stopping criterion allows us to optimize the process, stopping the process once there is nothing more to discover. As shown in the histogram in Fig. 6, the need for additional refinement decreases after each iteration, with 15% of cases requiring no refinement at all. Given the diverging sensitivity and PPV indicated in in Fig. 5, we set a hard limit of 10 refinement steps. This is also visible in the histogram through the clustering in the last bar of all the cases demanding

TABLE IV

RUNTIME COMPARISON FOR ONE ITERATION ON INPUT OF SHAPE (512,512,235). EXPLAINABILITY PIPELINE, BASED ON INTEGRATED GRADIENTS (IG), RUNTIME IS SIGNIFICANTLY LARGER THAN THE RUNTIME OF THE DEEP LEARNING (DL) PIPELINE. WHILE THE RUNTIME IS STILL ACCEPTABLE FOR ACTING AS AN OFFLINE TEACHER, IT WOULD BE UNACCEPTABLE FOR DEPLOYMENT SCENARIOS. ADDITION OF MULTI REFERENCE IG INCREASES RUNTIME 3 FOLD, AND ADDITION OF NOISY SAMPLE AVERAGING AN ADDITIONAL 1.5 FOLD. UNFORTUNATELY NOISY SAMPLE AVERAGING DOES NOT PROVIDE ANY SIGNIFICANT PERFORMANCE INCREASE, AND IS NOT ADOPTED IN FINAL PIPELINE. NOTE: RUNTIMES DO NOT SCALE LINEARLY DUE TO OTHER OPERATIONS BESIDES THE INFERENCE ITSELF.

Model	References	Noisy Samples	Time (s)	F1
IG	1	-	62.5	63.8
IG	5	-	190.5	64.4
IG	5	5	289.8	64.5
DL	-	-	3.7	71.6

more than 10 refinement steps.

An example of additional PE discovery via refinement is also displayed in Fig. 3.

Prediction filtering. In Table III we show that the F1 score can be greatly improved through postprocessing of the predicted clusters. By filtering all clusters based on their size and location, F1 is improved by 10.8%. This improvement is maximized by setting the initial operating point of the pipeline to a high sensitive one, opting to have candidate PEs which we filter afterwards. In our experiments, we filtered anything with distance from center greater than 160 pixels, and with size in voxels lower than 100. The distance filter corresponds to the lung area in most patients, and the size filter to very small clusters.

Pipeline runtime. An important factor in medical machine learning application is the runtime of the pipelines created, which determines how said pipelines can be adopted by the clinical field. In table IV we measure the runtime of our pipeline and we show that adoption of a third stage is critical for any deployment scenario, both in terms of both performance and speed. We report runtime for our deep learning segmentation model, and integrated gradients, both baseline setting and voting settings using multiple references and multiple noisy inputs. We show that additional references bring an improvement of 0.6% F1 score, however at a runtime 3 times higher. However averaging over inputs with added noise obtained only 0.1% additional F1 score at an 1,5 times increased runtime, so it was not used in final training. Finally, the deep learning method trained on the pseudo-labels was 50 times faster than its teacher model, while getting a 7.1% increase in F1. Testing was done on a NVIDIA RTX A4500.

C. Deep learning segmentation model.

For our final stage, we present model localization performance, results displayed in Table V. Our main comparison is another PE pipeline [33] that, the same as us, train on generated PE pseudo-labels on the same data from RSPECT dataset [50], however their dataset has a higher positivity of 31.0% than our 25.8% due to us removing the RSPECT

TABLE V

DEEP LEARNING MODEL PERFORMANCE. WE REPORT OUR PERFORMANCE ON TWO DATASETS OF 6,824 AND 13,329 CTPA STUDIES. COMPARING WITH OTHER PSEUDO-LABEL METHODS [33] TRAINED ON A SIMILAR DATASET, WE OBTAIN SLIGHTLY BETTER PERFORMANCE. BY ADDING MORE PRIVATE DATA TO THE TRAINING SET, PERFORMANCE SIMILAR TO STRONGLY SUPERVISED METHODS [39] EVALUATED USING THE SAME DETECTION MATCHING CRITERIA IS OBTAINED.

Model	Data	Positives	Recall	PPV	F1
Weakly Supervised Methods					
Pu et al [33]	6,415	1990	61.8	78.2	69.1
Our Model	6,824	1,766	61.5	79.6	69.4
	13,329	3,389	66.9	77.0	71.6
Strongly Supervised Methods					
Ozkan et al [32]	142	142	95.1	52.6	67.7
Tajbakhsh et al [65]	121	121	83.4	47.2	60.3
Tajbakhsh et al [66]	121	121	32.9	98.6	49.4
Xu et al [40]	113	113	93.2	51.2	66.1
Zhu et al [39]	142	142	86	61.3	71.6
Weikert et al [28]	30,000	15,858	82.2	86.8	85.8

TABLE VI

STRONGLY SUPERVISED TRAINING RESULTS. WE TRAIN OUR MODEL ON HUMAN ANNOTATION, STARTING FROM BOTH RANDOM INITIALIZATION AND WEAKLY SUPERVISED PRETRAINED WEIGHTS. FINETUNNING THE MODEL TRAINED ON PSEUDO-LABELS OBTAINS A PERFORMANCE BOOST OF 3.9 % F1 SCORE, IMPROVING BOTH SENSITIVITY AND PPV. THE FINETUNNED MODEL ALSO OUTPERFORMS RANDOM INITIALIZATION BY 4.5 % F1 AND ANOTHER STRONGLY SUPERVISED METHOD TRAINED ON SIMILAR AMOUNT OF DATA [39]. OUR WSL MODEL IN ITALICS IS TRAINED ON PSEUDO-LABELS, AND ADDED FOR EASIER VISUALIZATION OF THE IMPROVEMENT OBTAINED THROUGH FINETUNNING.

Model	Data	Positives	Recall	PPV	F1
<i>Our WSL model</i>	<i>13,329</i>	<i>3,389</i>	<i>66.9</i>	<i>77.0</i>	<i>71.6</i>
<i>Baseline</i>					
Zhu et al [39]	142	142	86.0	61.3	71.6
Our Random Init	111	111	66.2	76.6	71.0
Our WSL model	111	111	73.9	77.5	75.5
Finetunned					

augmented [34] from our training data. When trained on similar data volumes, we obtain an improvement of 0.3% F1 score, obtaining F1 scores of 69.4% compared to their 69.1%. We also augment our train data using private data, and obtain 71.6% F1 score, an increase of 2.2%.

We also compare with fully supervised methods trained on human made annotations [28], [39], [40]. We directly compare with Zhu et al [39] on the same matching metric. They also utilize a different subset of RSPECT [50], indicating a similar data distribution. We obtain the same F1 score performance of 71.6%. While they train on much less data, although human annotated, they also rely on additional models to generate pulmonary artery segmentation, helping exclude common False Positive cases of PEs detected outside the arteries [28].

Strongly supervised finetune. To further demonstrate the capabilities of our weakly supervised pipeline, we further finetune the model on human annotations. We train on 25% of RSPECT Augmented, 111 studies, a similar supervised amount to Zhu et al [39], allowing for direct comparison. For better evaluation of our performance contribution, we train our deep learning from scratch on the same data. This would allow the disentanglement of performance boost brought by human labels from the boost brought from the contribution of other methods.

We rely on straight forward finetuning of the model trained on explainability generated pseudo-labels, targeting the most common scenario. In this scenario, we show that our weakly supervised training can also act as a pretraining. Through simple finetuning we obtain a performance boost of 3.9 % F1 score, improving both sensitivity and PPV. The finetuned model also outperforms 3.9 % F1 score a more complex well designed pipeline [39] trained on a similar amount of data.

Additionally, we train our deep learning network starting from He initialization [67], and obtain an F1 of 71.0%, lower by 4.5% F1 than the model also pretrained on pseudo-labels. This indicates that our weakly supervised learning pipeline is also a strong pretraining strategy. This has very practical benefits for our context, since it allows a strong model to be developed starting from coarse annotations, and to be further improved once fine grained human annotations are obtained. Detailed results are displayed in Table VI.

Training Details. A shorter training schedule for finetuning is adopted, with 10.000 iterations with a batch size of 32 using the AdadW optimizer [55], with a starting learning rate of 1e-5, a warm up of 200 iterations and linear decay to 1e-7. For random initialization training, an intermediate length schedule of 25.000 iterations was adopted, with a starting learning rate of 1e-4, a warm up of 500 iterations, and linear decay to 1e-7.

Error Analysis Similar to other PE detection methods [28], [39], our model is also impacted by difficult cases. Regarding False Positives, common fail cases, also reported by related work, are due to contrast issues, imaging artifacts, and mistaking pulmonary veins for pulmonary arteries. For False Negative cases, no clear patterns were observed. Qualitative examples of errors are presented in Fig 7.

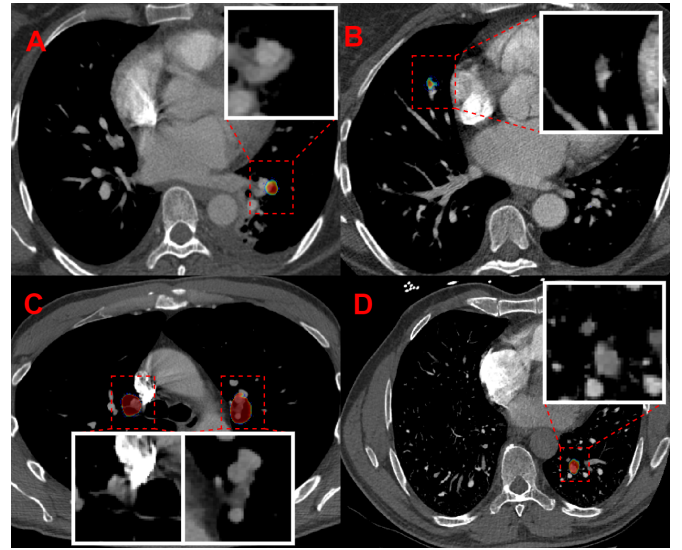


Fig. 7. Qualitative Error Examples. For PE detection, certain anatomical and imaging features are common False Positive factors. A) Reduced contrast in a vein adjacent to an artery is mistaken for a PE. B) Veins in study have a high contrast due to poor timing, causing model to mistake the vein for an artery. C) Image Left: Shadows due to imaging artifact, Image Right: vein mistaken for an artery. D) Vein mistaken for an artery.

V. CONCLUSIONS

In this paper, we demonstrate the effectiveness of a general weakly supervised pipeline, capable of increasing the granularity level of annotations by leveraging model explainability. We give a detailed experimented recipe on designing such a pipeline to be adopted on future similar task, to further encourage reuse and upgrading of already existing annotations. Expanding upon previous work [44], we also show that the signal contained by our pseudo-labels is rich and consistent enough to obtain performance comparable to models trained on human annotations, displaying the great potential of this direction of research.

Disclaimer: The concepts and information presented in this paper/presentation are based on research results that are not commercially available. Future commercial availability cannot be guaranteed.

REFERENCES

- [1] G. E. Raskob, P. Anghchaisuksiri, A. N. Blanco, H. Buller, A. Gallus, B. J. Hunt, E. M. Hylek, A. Kakkar, S. V. Konstantinides, M. McCumber *et al.*, "Thrombosis: a major contributor to global disease burden," *Arteriosclerosis, thrombosis, and vascular biology*, vol. 34, no. 11, pp. 2363–2371, 2014.
- [2] K. Keller, L. Hobohm, M. Ebner, K.-P. Kresoja, T. Münzel, S. V. Konstantinides, and M. Lankeit, "Trends in thrombolytic treatment and outcomes of acute pulmonary embolism in germany," *European heart journal*, vol. 41, no. 4, pp. 522–529, 2020.
- [3] A. M. Wendelboe and G. E. Raskob, "Global burden of thrombosis: epidemiologic aspects," *Circulation research*, vol. 118, no. 9, pp. 1340–1347, 2016.
- [4] I. Katsoularis, O. Fonseca-Rodríguez, P. Farrington, H. Jerndal, E. H. Lundevaller, M. Sund, K. Lindmark, and A. M. F. Connolly, "Risks of deep vein thrombosis, pulmonary embolism, and bleeding after covid-19: nationwide self-controlled cases series and matched cohort study," *BMJ*, vol. 377, p. e069590, 4 2022. [Online]. Available: <https://www.bmj.com/content/377/bmj-2021-069590><https://www.bmj.com/content/377/bmj-2021-069590.abstract>
- [5] P. Lehnert, T. Lange, C. H. Möller, P. S. Olsen, and J. Carlsen, "Acute pulmonary embolism in a national danish cohort: increasing incidence and decreasing mortality," *Thrombosis and haemostasis*, vol. 118, no. 03, pp. 539–546, 2018.
- [6] F. Dentali, W. Ageno, F. Pomero, L. Fenoglio, A. Squizzato, and M. Bonzini, "Time trends and case fatality rate of in-hospital treated pulmonary embolism during 11 years of observation in northwestern italy," *Thrombosis and haemostasis*, vol. 115, no. 02, pp. 399–405, 2016.
- [7] J. de Miguel-Díez, R. Jiménez-García, D. Jiménez, M. Monreal, R. Guijarro, R. Otero, V. Hernández-Barrera, J. Trujillo-Santos, A. L. de Andrés, and P. Carrasco-Garrido, "Trends in hospital admissions for pulmonary embolism in spain from 2002 to 2011," *European Respiratory Journal*, vol. 44, no. 4, pp. 942–950, 2014.
- [8] A. T. Cohen, G. Agnelli, F. A. Anderson, J. I. Arcelus, D. Bergqvist, J. G. Brecht, I. A. Greer, J. A. Heit, J. L. Hutchinson, A. K. Kakkar *et al.*, "Venous thromboembolism (vte) in europe," *Thrombosis and haemostasis*, vol. 98, no. 10, pp. 756–764, 2007.
- [9] K. E. Kocher, W. J. Meurer, R. Fazel, P. A. Scott, H. M. Krumholz, and B. K. Nallamothu, "National trends in use of computed tomography in the emergency department," *Annals of emergency medicine*, vol. 58, no. 5, pp. 452–462, 2011.
- [10] I. Portoghese, M. Galletta, R. C. Coppola, G. Finco, and M. Campagna, "Burnout and workload among health care workers: the moderating role of job control," *Safety and health at work*, vol. 5, no. 3, pp. 152–157, 2014.
- [11] S. A. Oldham *et al.*, "Ctpa as the gold standard for the diagnosis of pulmonary embolism," *International Journal of Computer Assisted Radiology and Surgery*, vol. 6, no. 4, pp. 557–563, 2011.
- [12] Y. LeCun, L. Bottou, Y. Bengio, and P. Haffner, "Gradient-based learning applied to document recognition," *Proceedings of the IEEE*, vol. 86, no. 11, pp. 2278–2324, 1998.
- [13] A. Krizhevsky, I. Sutskever, and G. E. Hinton, "Imagenet classification with deep convolutional neural networks," *Communications of the ACM*, vol. 60, no. 6, pp. 84–90, 2017.
- [14] K. Simonyan and A. Zisserman, "Very deep convolutional networks for large-scale image recognition," in *iclr*. Computational and Biological Learning Society, 2015, pp. 1–14.
- [15] O. Ronneberger, P. Fischer, and T. Brox, "U-net: Convolutional networks for biomedical image segmentation," in *International Conference on Medical image computing and computer-assisted intervention*. Springer, 2015, pp. 234–241.
- [16] T. T. Ho, T. Kim, W. J. Kim, C. H. Lee, K. J. Chae, S. H. Bak, S. O. Kwon, G. Y. Jin, E.-K. Park, and S. Choi, "A 3d-cnn model with ct-based parametric response mapping for classifying copd subjects," *Scientific Reports*, vol. 11, no. 1, pp. 1–12, 2021.
- [17] M. Polsinelli, L. Cinque, and G. Placidi, "A light cnn for detecting covid-19 from ct scans of the chest," *Pattern recognition letters*, vol. 140, pp. 95–100, 2020.
- [18] L. M. Prevedello, B. S. Erdal, J. L. Ryu, K. J. Little, M. Demirer, S. Qian, and R. D. White, "Automated critical test findings identification and online notification system using artificial intelligence in imaging," *Radiology*, vol. 285, no. 3, pp. 923–931, 2017.
- [19] S. Soffer, A. Ben-Cohen, O. Shimon, M. M. Amitai, H. Greenspan, and E. Klang, "Convolutional neural networks for radiologic images: a radiologist's guide," *Radiology*, vol. 290, no. 3, pp. 590–606, 2019.
- [20] R. Yamashita, M. Nishio, R. K. G. Do, and K. Togashi, "Convolutional neural networks: an overview and application in radiology," *Insights into imaging*, vol. 9, no. 4, pp. 611–629, 2018.
- [21] H. M. Ali, M. S. Kaiser, and M. Mahmud, "Application of convolutional neural network in segmenting brain regions from mri data," in *International conference on brain informatics*. Springer, 2019, pp. 136–146.
- [22] W. Lin, T. Tong, Q. Gao, D. Guo, X. Du, Y. Yang, G. Guo, M. Xiao, M. Du, X. Qu *et al.*, "Convolutional neural networks-based mri image analysis for the alzheimer's disease prediction from mild cognitive impairment," *Frontiers in neuroscience*, vol. 12, p. 777, 2018.
- [23] F. Isensee, P. F. Jaeger, S. A. A. Kohl, J. Petersen, and K. H. Maier-Hein, "Automated design of deep learning methods for biomedical image segmentation," *arxiv*, 2019.
- [24] O. Ronneberger, P. Fischer, and T. Brox, "U-net: Convolutional networks for biomedical image segmentation," *Medical Image Computing and Computer-Assisted Intervention—MICCAI 2015*, pp. 234–241, 2015.
- [25] F. Milletari, N. Navab, and S.-A. Ahmadi, "V-net: Fully convolutional neural networks for volumetric medical image segmentation," *2016 Fourth International Conference on 3D Vision (3DV)*, pp. 565–571, 2016.
- [26] A. B. Cheikh, G. Gorincour, H. Nivet, J. May, M. Seux, P. Calame, V. Thomson, E. Delabrousse, and A. Crombé, "How artificial intelligence improves radiological interpretation in suspected pulmonary embolism," *European Radiology*, pp. 1–12, 3 2022.
- [27] S. Soffer, E. Klang, O. Shimon, Y. Barash, N. Cahan, H. Greenspan, and E. Konen, "Deep learning for pulmonary embolism detection on computed tomography pulmonary angiogram: a systematic review and meta-analysis," *Scientific Reports 2021 11:1*, vol. 11, pp. 1–8, 8 2021. [Online]. Available: <https://www.nature.com/articles/s41598-021-95249-3>
- [28] T. Weikert, D. J. Winkel, J. Bremerich, B. Stieltjes, V. Parmar, A. W. Sauter, and G. Sommer, "Automated detection of pulmonary embolism in ct pulmonary angiograms using an ai-powered algorithm," *European radiology*, vol. 30, pp. 6545–6553, 12 2020. [Online]. Available: <https://pubmed.ncbi.nlm.nih.gov/32621243/>
- [29] S. C. Huang, T. Kothari, I. Banerjee, C. Chute, R. L. Ball, N. Borus, A. Huang, B. N. Patel, R. Rajpurkar, J. Irvin, J. Dunmon, J. Bledsoe, K. Shpanskaya, A. Dhaliwal, R. Zamanian, A. Y. Ng, and M. P. Lungren, "Penet—a scalable deep-learning model for automated diagnosis of pulmonary embolism using volumetric ct imaging," *npj Digital Medicine 2020 3:1*, vol. 3, pp. 1–9, 4 2020. [Online]. Available: <https://www.nature.com/articles/s41746-020-0266-y>
- [30] X. Ma, E. C. Ferguson, X. Jiang, S. I. Savitz, and S. Shams, "A multitask deep learning approach for pulmonary embolism detection and identification," *Scientific Reports 2022 12:1*, vol. 12, pp. 1–11, 7 2022. [Online]. Available: <https://www.nature.com/articles/s41598-022-16976-9>
- [31] F. Condrea, S. Rapaka, L. Itu, P. Sharma, J. Sperl, A. M. Ali, and M. Leordeanu, "Anatomically aware dual-hop learning for pulmonary embolism detection in ct pulmonary angiograms," *arXiv preprint arXiv:2303.17593*, 2023.
- [32] H. Özkan, O. Osman, S. Şahin, and A. F. Boz, "A novel method for pulmonary embolism detection in cta images," *Computer methods and programs in biomedicine*, vol. 113, no. 3, pp. 757–766, 2014.
- [33] J. Pu, N. S. Gezer, S. Ren, A. O. Alpaydin, E. R. Avci, M. G. Risbano, B. Rivera-Lebron, S. Y.-W. Chan, and J. K. Leader, "Automated detection and segmentation of pulmonary embolisms on computed tomography pulmonary angiography (ctpa) using deep learning but without manual outlining," *Medical Image Analysis*, vol. 89, p. 102882, 2023.
- [34] M. F. Callejas, H. M. Lin, T. Howard, M. Aitken, M. Napoleone, L. Jimenez-Juan, R. Moreland, S. Mathur, D. P. Deva, and E. Colak, "Augmentation of the rsna pulmonary embolism ct dataset with bounding box annotations and anatomic localization of pulmonary emboli," *Radiology: Artificial Intelligence*, vol. 5, no. 3, p. e230001, 2023.
- [35] C. Zhou, H. P. Chan, B. Sahiner, L. M. Hadjiiski, A. Chughtai, S. Patel, J. Wei, P. N. Cascade, and E. A. Kazerooni, "Computer-aided detection of pulmonary embolism in computed tomographic pulmonary angiography (ctpa): Performance evaluation with independent data sets," *Medical Physics*, vol. 36, p. 3385, 2009. [Online]. Available: <https://pubmed.ncbi.nlm.nih.gov/19495/>
- [36] H. Bouma, J. J. Sonnemans, A. Vilanova, and F. A. Gerritsen, "Automatic detection of pulmonary embolism in cta images," *IEEE Transactions on Medical Imaging*, vol. 28, pp. 1223–1230, 8 2009.
- [37] E. Pichon, C. L. Novak, A. P. Kiraly, and D. P. Naidich, "A novel method for pulmonary emboli visualization from high-resolution ct images,"

- Medical Imaging 2004: Visualization, Image-Guided Procedures, and Display*, vol. 5367, p. 161, 5 2004.
- [38] J. Liang and J. Bi, "Computer aided detection of pulmonary embolism with tobogganing and mutple instance classification in ct pulmonary angiography," *Information processing in medical imaging : proceedings of the ... conference*, vol. 20, pp. 630–641, 2007. [Online]. Available: <https://pubmed.ncbi.nlm.nih.gov/17633735/>
- [39] H. Zhu, G. Tao, Y. Jiang, L. Sun, J. Chen, J. Guo, N. Wang, H. Wei, X. Liu, Y. Chen *et al.*, "Automatic detection of pulmonary embolism on computed tomography pulmonary angiogram scan using a three-dimensional convolutional neural network," *European Journal of Radiology*, p. 111586, 2024.
- [40] H. Xu, H. Li, Q. Xu, Z. Zhang, P. Wang, D. Li, and L. Guo, "Automatic detection of pulmonary embolism in computed tomography pulmonary angiography using scaled-yolov4," *Medical Physics*, vol. 50, no. 7, pp. 4340–4350, 2023.
- [41] M. Sundararajan, A. Taly, and Q. Yan, "Axiomatic attribution for deep networks," in *International conference on machine learning*. PMLR, 2017, pp. 3319–3328.
- [42] R. R. Selvaraju, M. Cogswell, A. Das, R. Vedantam, D. Parikh, and D. Batra, "Grad-cam: Visual explanations from deep networks via gradient-based localization," in *Proceedings of the IEEE international conference on computer vision*, 2017, pp. 618–626.
- [43] D. Smilkov, N. Thorat, B. Kim, F. Viégas, and M. Wattenberg, "Smoothgrad: removing noise by adding noise," *arXiv preprint arXiv:1706.03825*, 2017.
- [44] C. González-Gonzalo, B. Liefers, B. van Ginneken, and C. I. Sánchez, "Iterative augmentation of visual evidence for weakly-supervised lesion localization in deep interpretability frameworks: application to color fundus images," *IEEE transactions on medical imaging*, vol. 39, no. 11, pp. 3499–3511, 2020.
- [45] M. Fröh, M. Fischer, A. Schilling, S. Gatidis, and T. Hepp, "Weakly supervised segmentation of tumor lesions in pet-ct hybrid imaging," *Journal of Medical Imaging*, vol. 8, no. 5, pp. 054003–054003, 2021.
- [46] H. Yang, C. Shan, A. F. Kolen, and P. H. de With, "Weakly-supervised learning for catheter segmentation in 3d frustum ultrasound," *Computerized Medical Imaging and Graphics*, vol. 96, p. 102037, 2022.
- [47] H.-G. Nguyen, A. Pica, J. Hrbacek, D. C. Weber, F. La Rosa, A. Schalenbourg, R. Sznitman, and M. B. Cuadra, "A novel segmentation framework for uveal melanoma in magnetic resonance imaging based on class activation maps," in *International Conference on Medical Imaging with Deep Learning*. PMLR, 2019, pp. 370–379.
- [48] X. Guanshuo, "1st place solution," Apr 2018. [Online]. Available: <https://www.kaggle.com/shadowwarrior/1st-place-solution>
- [49] N. Thanh Dat, "Rrna str pulmonary embolism detection," 2020. [Online]. Available: <https://www.kaggle.com/c/rsna-str-pulmonary-embolism-detection/discussion/193424>
- [50] E. Colak, F. C. Kitamura, S. B. Hobbs, C. C. Wu, M. P. Lungren, L. M. Prevedello, J. Kalpathy-Cramer, R. L. Ball, G. Shih, A. Stein, S. S. Halabi, E. Altinmakas, M. Law, P. Kumar, K. A. Manzalawi, D. C. Nelson Rubio, J. W. Sechrist, P. Germaine, E. C. Lopez, T. Amerio, G. Gupta, M. Jain, F. U. Kay, C. T. Lin, S. Sen, J. W. Revels, C. C. Brussaard, J. Mongan, N. Abdala, B. Bearce, H. Carrete, H. Dogan, S.-C. Huang, P. Crivellaro, S. Dincler, H. Kavnoudias, R. Lee, H.-M. Lin, H. Salehinejad, O. Samorodova, E. Rodrigues dos Santos, J. Seah, A. Zia, V. A. Arteaga, K. Batra, A. Castelli von Atzingen, A. Chacko, P. B. DiDomenico, R. R. Gill, M. A. Hafez, S. John, R. L. Karl, J. P. Kanne, R. V. Mathilakath Nair, S. McDermott, P. K. Mittal, A. Mumbower, C. Lee, P. J. Oraisclio, D. Palacio, C. Pozzessere, P. Rajiah, O. A. Ramos, S. Rodriguez, M. N. Shaaban, P. N. Shah, H. Son, S. K. Sonavane, B. Spieler, E. Tsai, A. Vásquez, D. Vijayakumar, P. P. Wali, A. Wand, and G. E. Zamora Endara, "The rsna pulmonary embolism ct dataset," *Radiology: Artificial Intelligence*, vol. 3, no. 2, p. e200254, 2021, pMID: 33937862. [Online]. Available: <https://doi.org/10.1148/ryai.2021200254>
- [51] R. Solovyev, A. A. Kalinin, and T. Gabruseva, "3d convolutional neural networks for stalled brain capillary detection," *Computers in biology and medicine*, vol. 141, p. 105089, 2022.
- [52] H. Zhang, M. Cisse, Y. N. Dauphin, and D. Lopez-Paz, "mixup: Beyond empirical risk minimization," *arXiv preprint arXiv:1710.09412*, 2017.
- [53] T. Ridnik, E. Ben-Baruch, A. Noy, and L. Zelnik-Manor, "Imagenet-21k pretraining for the masses," *arXiv preprint arXiv:2104.10972*, 2021.
- [54] R. Wightman, "Pytorch image models," <https://github.com/rwightman/pytorch-image-models>, 2019.
- [55] I. Loshchilov, "Decoupled weight decay regularization," *arXiv preprint arXiv:1711.05101*, 2017.
- [56] N. Kokhlikyan, V. Miglani, M. Martin, E. Wang, B. Alsallakh, J. Reynolds, A. Melnikov, N. Kliushkina, C. Araya, S. Yan, and O. Reblitz-Richardson, "Captum: A unified and generic model interpretability library for pytorch," 2020.
- [57] K. Simonyan, "Deep inside convolutional networks: Visualising image classification models and saliency maps," *arXiv preprint arXiv:1312.6034*, 2013.
- [58] J. T. Springenberg, A. Dosovitskiy, T. Brox, and M. Riedmiller, "Striving for simplicity: The all convolutional net," *arXiv preprint arXiv:1412.6806*, 2014.
- [59] C. Wittram, "How i do it: Ct pulmonary angiography," *American journal of roentgenology*, vol. 188, no. 5, pp. 1255–1261, 2007.
- [60] P. Sturmflus, S. Lundberg, and S.-I. Lee, "Visualizing the impact of feature attribution baselines," *Distill*, vol. 5, no. 1, p. e22, 2020.
- [61] M. J. Cardoso, A. Feragen, B. Glocker, E. Konukoglu, I. Oguz, J. Petersen, M. D. Schirmer, and G. Langs, "Monai: An open-source framework for deep learning in healthcare," *Nature Methods*, vol. 19, no. 12, pp. 1583–1585, 2022.
- [62] C. H. Sudre, W. Li, T. Vercauteren, S. Ourselin, and M. J. Cardoso, "Generalised dice overlap as a deep learning loss function for highly unbalanced segmentations," in *Deep learning in medical image analysis and multimodal learning for clinical decision support*. Springer, 2017, pp. 240–248.
- [63] M. Anouk Stein, C. Wu, C. Carr, E. Colak, G. Shih, Jeff Rudie, J. Mongan, J. Elliott, L. Prevedello, M. Marc Kohli, P. Culliton, and R. Ball, "Rrna str pulmonary embolism detection," <https://kaggle.com/competitions/rsna-str-pulmonary-embolism-detection>, 2020, kaggle.
- [64] P. Ajmera, A. Kharat, J. Seth, S. Rathi, R. Pant, M. Gawali, V. Kulkarni, R. Maramraju, I. Kedia, R. Botchu *et al.*, "A deep learning approach for automated diagnosis of pulmonary embolism on computed tomographic pulmonary angiography," *BMC Medical Imaging*, vol. 22, no. 1, p. 195, 2022.
- [65] N. Tajbakhsh, M. B. Gotway, and J. Liang, "Computer-aided pulmonary embolism detection using a novel vessel-aligned multi-planar image representation and convolutional neural networks," in *Medical Image Computing and Computer-Assisted Intervention–MICCAI 2015: 18th International Conference, Munich, Germany, October 5–9, 2015, Proceedings, Part II 18*. Springer, 2015, pp. 62–69.
- [66] N. Tajbakhsh, J. Y. Shin, M. B. Gotway, and J. Liang, "Computer-aided detection and visualization of pulmonary embolism using a novel, compact, and discriminative image representation," *Medical image analysis*, vol. 58, p. 101541, 2019.
- [67] K. He, X. Zhang, S. Ren, and J. Sun, "Delving deep into rectifiers: Surpassing human-level performance on imagenet classification," in *Proceedings of the IEEE international conference on computer vision*, 2015, pp. 1026–1034.